Environmental Science Advances

ROYAL SOCIETY OF CHEMISTRY

PAPER

View Article Online
View Journal | View Issue



Cite this: *Environ. Sci.: Adv.*, 2024, **3**, 925

# Proficient Engineering of NiO/$Cu_2S$/rGO heterojunction photocatalysts: fabrication, dye degradation, and mechanism pathways towards environmental remediation

Balaji Parasuraman,[a] Paramasivam Shanmugam,[b] Sambasivam Sangaraju,[c] Hariprasath Rangaraju,[a] Dhayal Raj Alphonse,[d] Mohammed Nawaz Husain[a] and Pazhanivel Thangavelu *[a]

Contemporary fashion industry uses numerous dyes and global attention has been drawn to the widespread use, toxicity, carcinogenicity, and bioaccumulation of mixed dyes. Therefore, researchers and scientists are focused on using broad spectrum of photocatalysts to achieve dye remediation with maximum efficiency. Herein, we report the fabrication of novel NiO/$Cu_2S$/rGO ternary nanocomposites synthesized *via* the one-step hydrothermal method. The as-synthesized sample was analyzed by applying different analytical techniques, such as XRD, FTIR, UV-DRS, SEM, EDX, elemental mapping, and HRTEM analyses. The results confirmed that the NiO and $Cu_2S$ nanoparticles are decorated on the 2D-rGO nanosheets. An interfacial ternary heterostructure was successfully utilized for the photocatalytic environmental remediation of mixed dye pollutants under UV-light irradiation. Several key factors contribute to the remarkable photocatalytic performance of these heterostructures, including the wide spectrum of the harvested light, good charge separation, and rapid charge transport. The optimized NiO/$Cu_2S$/rGO ternary nanocomposites exhibited the highest degradation efficiency of 92.4%, 97.9% and 91.6% for RhB, MB and mixed (RhB and MB) dyes, respectively. In contrast, the tentative photocatalytic mechanism pathway, scavengers experiments, recyclability and stability were also investigated. The results reveal that ($*O_2^-$) and *OH radical species play a major role under UV-light irradiation. The NiO/$Cu_2S$/rGO ternary nanocomposites have potential for the effective degradation of organic dyes in industrial wastewater and environmental remediation.

Received 4th December 2023
Accepted 2nd May 2024

DOI: 10.1039/d3va00368j

rsc.li/esadvances



## Environmental significance

The widespread presence of toxic dyes in wastewater has sparked global concern regarding their harmful effects on non-target organisms and human health. The protection of the environment is an inevitable global concern. Currently, there are a wide range of industries, such as textile, cosmetic, food processing, papermaking, and plastic industries, that use dyes. Globally, more than 700 000 metric tons of toxic pollutans are produced by textile companies. It is important to note that textile dyes negatively affect the aesthetic quality of waterbodies; increase biochemical and chemical oxygen demands; inhibit photosynthesis; enter the food chain; are recalcitrant and cause bioaccumulation; and may lead to toxicity, mutagenicity, and carcinogenicity. Therefore, we introduce a novel approach of creating and designing photocatalytic structures that align with the redox potentials of both reactive oxygen species (ROS) and mixed organic dyes. Thus, the ternary NiO/$Cu_2S$/rGO nanocomposite exhibited excellent visible light photocatalytic activity and good stability. This study suggests that NiO/$Cu_2S$/rGO ternary nanocomposites may be useful for dye degradation and deliver low-cost, environmentally friendly, clean drinking water without toxic dyes.

## 1. Introduction

In recent years, environmental pollution comprising water, air, and land pollution has become a worldwide problem that seriously endangers the health of all organisms on the planet, including humans.[1] In the last few decades, dyes in wastewater have produced serious environmental issues.[2] Numerous industries process materials using dyes, and it is estimated that 10–15% of the dyes used in the process are discharged in sewage during the dying process.[3] Exposure to these dyes may

[a]*Smart Material Laboratory, Department of Physics, Periyar University, Salem-636011, Tamil Nadu, India. E-mail: pazhanit@gmail.com*

[b]*Department of Chemistry, Faculty of Science and Technology, Thammasat University, Pathum Thani 12120, Thailand*

[c]*National Water and Energy Centre, United Arab Emirates University, Al Ain-15551, UAE*

[d]*Department of Physics, Sacred Heart College (Autonomous), Tirupattur 635601, Tamil Nadu, India*

cause skin irritation, eye irritation, and affect the functions of the kidneys, liver, brain, reproductive system, and central nervous system.[4,5] Particularly, methylene blue $C_{16}H_{18}ClN_3S$ is widely used in many textile industries.[6] Several techniques have been developed to effectively remove methylene blue, including ozonation,[7] extraction,[8] ion flotation,[9] ultrafiltration,[10] Fenton process,[11] sonolysis,[12] chemical coagulation,[13] adsorption,[14] flocculation,[15] oxidation,[16] and photocatalysis.[17,18] In photocatalytic technology, nano-scaled semiconductor materials have been widely used in recent years because of their low cost, easy synthesis, non-toxicity, and environmental friendliness.[19] Moreover, in the photocatalysis process, numerous essential aspects must be considered, including the band gap energy, effective surface area, light energy absorption characteristics, and optical properties of the photocatalytic materials[20] as well as the operation intensity, temperature, and pH of the photocatalytic degradation.[21] Semiconductor-based materials, such as ZnO,[23] NiO,[24] $Fe_2O_3$,[25] CuO,[26] $CoFe_2O_4$,[27] $NiFe_2O_4$,[28] and Cd-doped $SiO_2$,[29] have been widely used in the photocatalytic degradation process.[22] Based on the literature, NiO semiconductor materials are one of the significant photocatalyst materials because of their good chemical and physical properties and good stability. However, NiO has a wide bandgap energy owing to its relatively moderate visible light absorption ability and rapid photoelectron–hole pair recombination, and the photocatalytic efficiency of the NiO photocatalyst is of remarkable attention.

Recently, materials of the sulfide family (*e.g.*, $Bi_2S_3$, $Cu_2S$, $Ni_2S$, $MoS_2$, $SnS_2$, and $WS_2$) have been widely used in photocatalytic applications because of their good light response, fast electron–hole recombination and good stability.[30] For instance, Hong *et al.* used $Cu_2S$/g-$C_3N_4$ nanomaterials for photocatalytic application under UV light irradiation. Despite their good conductivity, precious metals are too expensive and scarce to be used widely.[31] In addition, carbon-based materials are broadly used in environmental applications, such as g-$C_3N_4$,[32] MWCNTs,[33] CNTs,[34] CNF[35] and rGO. Specifically, rGO is a significant promising material due to its potential application in photodegradation, $H_2$ production, energy conversion and $CO_2$ reduction. Furthermore, it is a promising option for visible light response photocatalysts because of its 2.2 eV band gap. In addition, due to its distinct electrical band structure, affordability and ease of fabrication, rGO has the potential to replace $TiO_2$ in solar energy applications. However, bare rGO still exhibits low photoactivity in several applications, such as water-splitting $H_2$ production and $CO_2$ reduction, due to the rapid recombination of photo-induced electron–hole pairs. For example, Wang *et al.* synthesized $NiCo_2O_4$/rGO photocatalysts prepared *via* a simple hydrothermal method for using $H_2$ evaluation under UV light irradiation. Therefore, a recent study aims to optimize the performance of the photocatalysts by coupling them together and by developing different charge transport models to improve their efficiency.

Based on the above consideration in this present work, NiO/$Cu_2S$/rGO heterostructured ternary nanocomposites were prepared using a simple one-step hydrothermal method and used for the photocatalytic degradation of dual dyes (MB and RhB). As a result of the increase in photocatalytic response sites, the optical absorption capability of the as-prepared nanocomposites was significantly enhanced. This study investigates contaminated waste water using a photocatalytic degradation process targeting two dyes: MB and RhB dyes. The possible photocatalytic degradation mechanism and scavenger test were also investigated in detail. It is noteworthy that this work offers helpful guidelines for creating heterojunction photocatalysts with visible light responses in an easy and ecologically friendly manner.

## 2. Experimental

### 2.1 Chemicals

Nickel nitrate hexahydrate [$Ni(NO_3)_2 \cdot 6H_2O$, 97%], sodium hydroxide (NaOH, 98%), thiourea [$CH_4N_2S$, 99%], sulphuric acid ($H_2SO_4$), copper nitrate [$Cu(NO_3)_2 \cdot 3H_2O$, 98%], sodium nitrate [$NaNO_3$, 98%], hydrochloric acid (HCl), ethanol [$C_2H_5OH$, 99%] and acetone [$CH_3COCH_3$, 99%] were purchased from Sigma-Aldrich Pvt. Ltd, Mumbai, India. All other compounds were used as obtained without purification. The reduced graphene oxide (rGO) was commercially purchased from Sigma-Aldrich Pvt. Ltd, Mumbai, India.

### 2.2 Preparation of NiO

In a typical synthesis, pure NiO nanoparticles were prepared using a simple hydrothermal method. A solution containing nickel nitrate and sodium hydroxide, ranging from 0.1 M of $Ni(NO_3)_2 \cdot 6H_2O$ to 0.8 M of NaOH, was stirred for 60 min. Subsequently, the pH of the solution was adjusted to 12, and the resulting solution was transferred to a 100 mL stainless-steel autoclave. The autoclave was heated at 120 °C overnight. Consequently, the obtained powder was calcinated at 600 °C for 5 h. Finally, the block-colored NiO nanoparticles were collected and used for further analysis.

### 2.3 Preparation of $Cu_2S$

The $Cu_2S$ nanoparticles were prepared using a simple hydrothermal method. Initially, 0.1 M of copper nitrate $Cu(NO_3)_2 \cdot 6H_2O$ and thiourea ($CH_4N_2S$) were dissolved in 100 mL deionized water (DDW). Subsequently, the colloidal solution was placed in a 100 mL Teflon-line steel reaction vessel and treated at 180 °C for 12 h in a hot air oven. Following the reaction, the precipitates were thoroughly cleaned by washing them with DDW and ethanol. Finally, the dried $Cu_2S$ powder was used for further analysis.

### 2.4 Preparation of ternary NiO/$Cu_2S$/rGO nanocomposites

NiO/$Cu_2S$/rGO ternary nanocomposites were prepared using the hydrothermal method. Initially, an equal amount of synthesized nanoparticles (NiO, $Cu_2S$ and rGO in a 1 : 1 : 1 ratio) were taken, and 15 mL of ethanol was added. The resulting solution was continuously stirred for 30 min, transferred into an autoclave and maintained at 80 °C for 12 h. The resulting NiO/$Cu_2S$/rGO ternary nanocomposites were collected and dried

 


Scheme 1 Schematic diagram of the synthesis procedure for the hybrid nanocomposites.

overnight. After drying, the nanocomposites were collected and stored for further experimental analysis (Scheme 1).

### 2.5 Material characterization

The crystalline structure and formation of the NiO/$Cu_2S$/rGO ternary nanocomposite were confirmed through X-ray diffraction (XRD) analysis conducted using a Rigaku Smart Lab diffractometer. The as-prepared samples were confirmed by Fourier-transform infrared spectroscopy (FTIR) using a PerkinElmer Fourier transform spectrometer to identify the corresponding functional groups. The morphology and elemental composition were analyzed by scanning electron microscopy (SEM) Carl Zeiss Sigma in Germany. Energy-dispersive X-ray spectroscopy (EDX) analysis was performed to determine the chemical composition of the ternary NiO/$Cu_2S$/rGO nanocomposite (FEI Quanta FEG 200 EDAX). High-resolution transmission electron microscopy (HR-TEM) using a JOEL JEM 2001 instrument was employed to investigate the morphology and confirm the heterojunction formation. The optical properties of the synthesized samples were assessed using UV-visible spectroscopy conducted using a PerkinElmer LAMBDA 950 UV-visible spectrophotometer.

### 2.6 Electrochemical measurements

The electrochemical measurements were studied on Biologic SP-150, an electrochemical workstation, to evaluate the electrochemical performance in a three-electrode system. The platinum wire, glassy carbon electrode (GCE), and Ag/AgCl were used as the counter, working, and reference electrodes, respectively.

### 2.7 Electrode fabrication

The previously prepared samples were dispersed in ethanol (5 mg $mL^{-1}$) and sonicated for 30 minutes. The optimized solution of colloidal $WO_3$/rGO nanocomposites (6 μL) was drop-coated on the GCE surface and dried at room temperature. Further electrochemical tests were performed using the modified electrode after the loosely bound particles were gently washed away with DI water.

### 2.8 Photocatalytic dye degradation experiments

The photocatalytic performance of the prepared nanocomposites was evaluated through the degradation of methylene blue (MB), rhodamine B (RhB) and mixed dye of methylene blue and rhodamine B (10 mg $L^{-1}$) using a 500 W Xe lamp and a cut-off filter ($\lambda > 420$ nm). Initially, a 100 mg photocatalyst was placed in 10 ppm of MB, RhB and mixed dye solution (100 mL) in three different borax glass tubes. Generally, the dye solutions were agitated for 30 min in the dark to reach adsorption–desorption equilibrium. One millilitre of the solution was then removed at predetermined time intervals and stored in a well plate. Then, they were analyzed using microplate reader techniques at the maximum adsorption wavelengths of MB and RhB dyes (664 and 463 nm, respectively). The degradation efficiency (%) of the dyes was estimated using the following formula:

$$\text{Degradation efficiency (\%)} = (C_0 - C)/C_0 \times 100,$$

where $C_0$ is the initial concentration of MB and RhB dyes and $C$ is the final concentration of the as-prepared dyes at time $t$.

### 2.9 Scavenger experiments

To determine the vital role of the active species in the degradation mechanism, different kinds of scavengers were tested in a dye solution (MB and RhB) before the reaction started. Isopropyl alcohol (IPA), ethylenediamine tetraacetic acid (EDTA), and benzoquinones (BQ) were used to identify hydroxyl radicals ($OH^-$), superoxide radicals ($O_2^*$) and holes ($h^+$) radicals, respectively. Trapping analysis was employed to assess photocatalytic activity under similar experimental conditions.

# 3. Results and discussion

## 3.1 Structural analysis

The crystalline structure and phase purity of the prepared samples were analyzed using X-ray diffraction analysis. The XRD patterns of the synthesized rGO, NiO, $Cu_2S$, NiO/$Cu_2S$, and NiO/$Cu_2S$/rGO ternary nanocomposite samples are displayed in Fig. 1(a). The diffraction pattern of the NiO closely matches the monoclinic structure of JCPDS card no. 04-0835,[36] with peaks observed at 19.56°, 29.41°, 33.26°, 38.05°, 59.19°, and 62.65° attributed to the planes of (311), (004), (002), (111), (200) and (220), respectively. Similarly, the diffraction pattern of the $Cu_2S$ confirms the hexagonal structure of standard JCPDS card no. 73-1138,[37] with peaks observed at 27.81°, 29.41°, 31.94°, 33.1°, 46.28°, 47.88°, 52.67°, and 59.46° attributed to the planes of (1 0 1), (1 0 2), (2 0 0), (1 0 3), (2 2 0), (1 1 0), (1 0 8) and (1 1 6), respectively. The peaks observed at 10.5° and 42.2° are attributed to the planes of (001) and (160), respectively, which are well matched with the standard JCPDS card number (75-2078).[38] In the binary composite NiO/$Cu_2S$, most peaks of both the NiO and $Cu_2S$ are visible, confirming successful composition. Similarly, in the case of the ternary composite NiO/$Cu_2S$/rGO, the peak at 42.2° confirms the presence of rGO in the composite. Furthermore, the addition of rGO nanosheets leads to a decrease in the intensity of the diffraction peaks around (1 6 0). The crystalline size of the prepared samples was calculated using Debye–Scherrer's equation. The sizes for rGO, NiO, $Cu_2S$, NiO/$Cu_2S$, and NiO/$Cu_2S$/rGO ternary nanocomposites are 18, 41, 25, 21 and 35 nm, respectively.

## 3.2 Functional group analysis

The surface composition and functional groups of the prepared samples were analyzed using FT-IR analysis. The obtained results for the prepared rGO, NiO, $Cu_2S$, NiO/$Cu_2S$ and NiO/$Cu_2S$/rGO ternary nanocomposite samples, recorded in the 4000–400 $cm^{-1}$ region at ambient temperature, are displayed in Fig. 1(b). All as-synthesized samples exhibited broadband at 3000–3500 $cm^{-1}$, which represents (O–H) stretching vibrations. Peaks around 2900 $cm^{-1}$ were visible in all the reported samples, indicating the presence of (C–H) stretching vibrations arising from hydrocarbon bon groups. Peaks at 1400 and 1200 $cm^{-1}$ were attributed to the (C–O and C=O, respectively) carboxylate stretching vibrational groups.[39] The spectral bands processed under 850 $cm^{-1}$ correspond to the metal–sulfide or metal–oxygen–metal and metal–oxygen (M = Ni, Cu). The ternary composite projects the availability of the characteristic bands corresponding to rGO, NiO, and $Cu_2S$, thereby authorizing the presence of all element counterparts and confirming the hybrid formation. The absence of intense transmission bands in the spectrum indicates the purity of the sample.

## 3.3 Optical properties

The optical absorption UV-DRS analysis played a significant role in the photocatalytic performance; thus, the as-synthesized samples were studied, as shown in Fig. 2(a). The absorption edges of the pure NiO, $Cu_2S$ and rGO samples were observed in the UV-visible region. However, the samples, after being combined with binary NiO/$Cu_2S$ and NiO/$Cu_2S$/rGO ternary nanocomposites, showed a smaller effect on shifting the absorption edges towards the UV-visible region. This small shift may be attributed to the strong interface interaction between rGO nanosheets and NiO/$Cu_2S$ nanocomposites. Based on the results obtained from the UV-vis DRS spectra, the indirect band gap of all the as-synthesized samples was measured using the Tauc plot. The calculated energy band gap values of the as-prepared samples, such as NiO, $Cu_2S$, rGO, NiO/$Cu_2S$ and NiO/$Cu_2S$/rGO ternary nanocomposites, are 3.57, 1.62, 2.45, 2.01 and 2.15 eV, respectively. The decrease in band gap can be attributed to the addition of the rGO, as clearly evident when comparing the bandgap values of the binary and ternary nanocomposites, as depicted in Fig. 2(b). The reduced bandgap leads to moderate electron–hole pair recombination, thereby enhancing the photocatalytic activity of the ternary NiO/$Cu_2S$/rGO nanocomposite. Thus, the NiO/$Cu_2S$/rGO ternary nanocomposite is expected to exhibit enhanced photocatalytic activity under UV-visible light irradiation.[40]

## 3.4 Morphology analysis

**3.4.1 SEM and EDX analysis.** The surface morphology of the NiO/$Cu_2S$/rGO ternary nanocomposites was directly

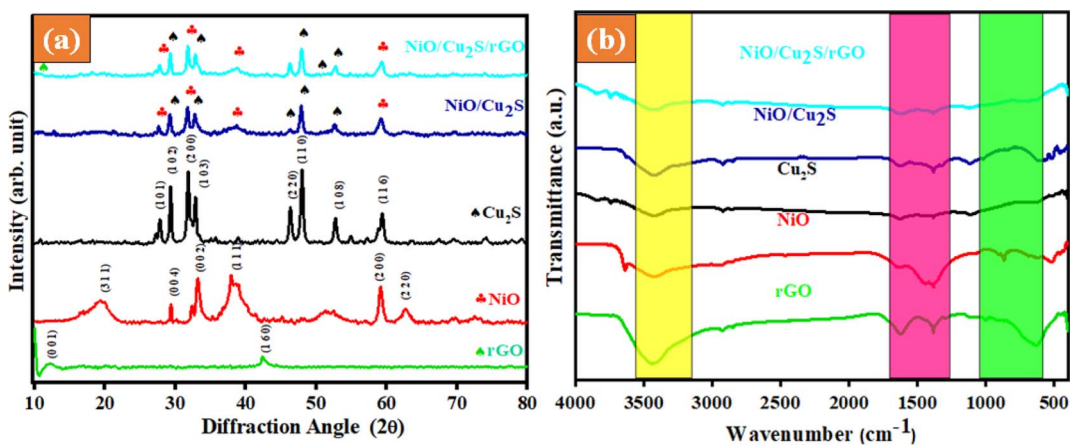


Fig. 1 (a) XRD pattern of the as-prepared samples. (b) FT-IR spectra of the as-prepared samples.

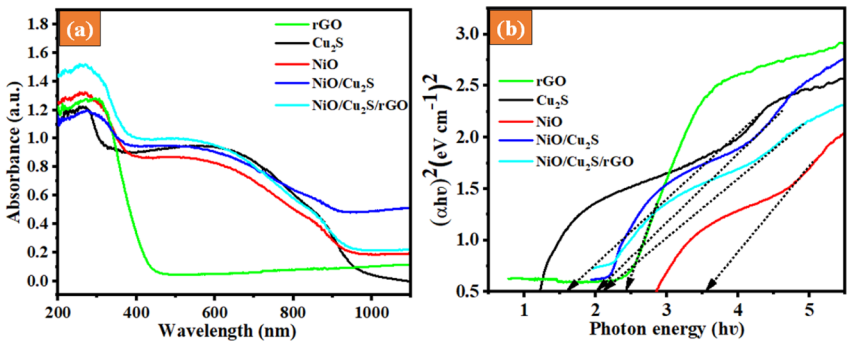


Fig. 2 (a) UV-visible absorption spectra of the as-prepared sample. (b) Band gap values from the Tauc plot of the as-prepared photocatalysts.

analyzed using SEM images. As depicted in Fig. 3(a)–(d), SEM images of the NiO/$Cu_2S$/rGO nanocomposite were displayed at different magnifications. The images clearly show the presence of a collection of $Cu_2S$ nanoparticles and NiO nanoparticles in the rGO nanosheets. The NiO/$Cu_2S$/rGO ternary nanocomposite was further analyzed by elemental mapping, as displayed in Fig. 3(e)–(j). The results suggest that NiO and $Cu_2S$ were uniformly distributed with the rGO nanosheets. As illustrated in Fig. 3(k), the EDX spectrum was processed for the hybrid ternary nanocomposite, demonstrating the sample's purity and providing the proper weight percentage of the available metals.

**3.4.2 HR-TEM analysis.** The internal morphology and structure of the NiO/$Cu_2S$/rGO ternary nanocomposite were analyzed using HR-TEM analysis. From the images, the formation of the nanocomposite was further confirmed, with the rGO nanosheets visible, as shown in Fig. 4(a). Fig. 4(b) demonstrates that the metal oxide and metal sulphide homogenously agglomerate on the rGO surface, and Fig. 4(c) shows that NiO and $Cu_2S$ nanoparticles are uniformly dispersed into the rGO nanosheet structure with dimensions of approximately 15–20 nm, which agrees with the measurements from Scherrer's equation. As depicted in Fig. 4(d), the SAED pattern of the synthesized NiO/$Cu_2S$/rGO ternary nanocomposite is displayed. From the image, it is visible that the nanocomposite resembles a polycrystalline nature. The HRTEM results confirm that the suggested interfacial force between the NiO, $Cu_2S$, and rGO

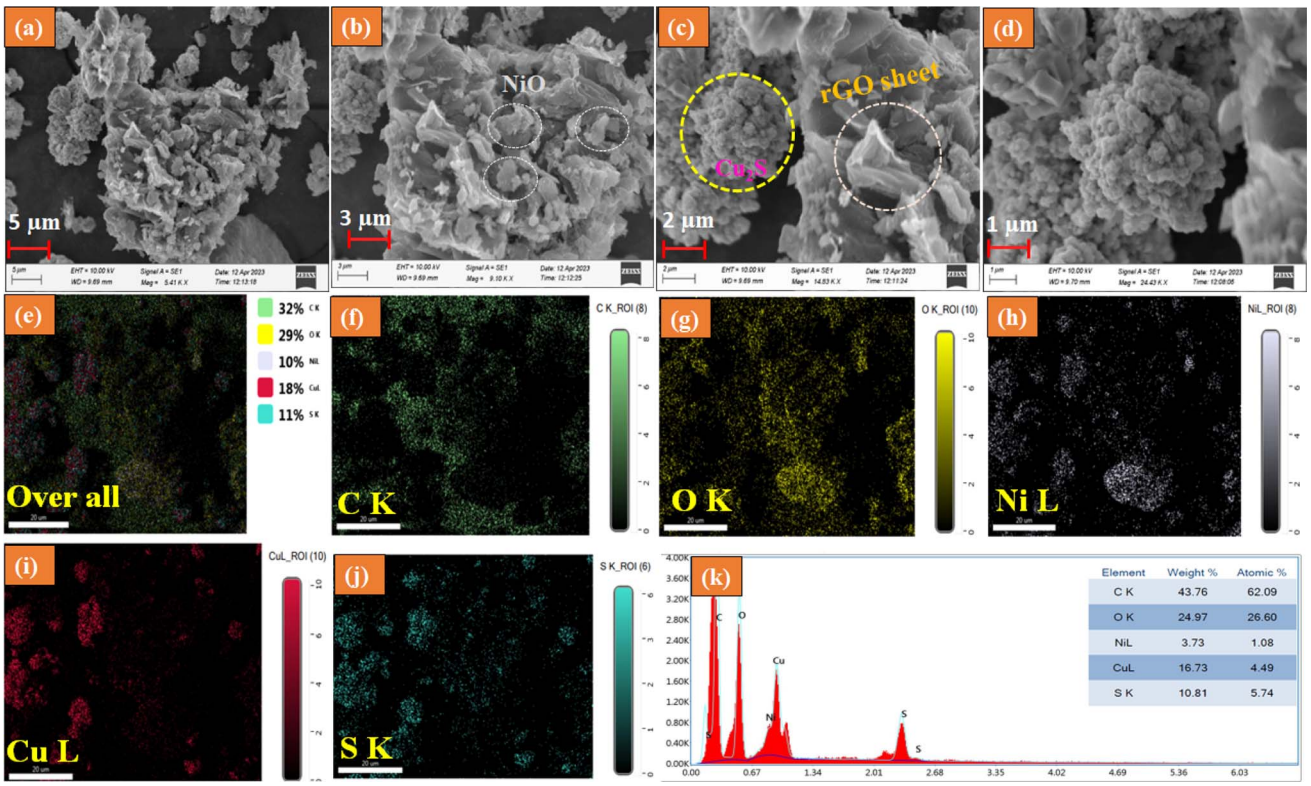


Fig. 3 (a)–(d) SEM images of the ternary composite NiO/$Cu_2S$/rGO processed at different magnifications, (e)–(j) mapping images of the ternary composite NiO/$Cu_2S$/rGO, and (k) EDX spectrum of the ternary nanocomposite sample NiO/$Cu_2S$/rGO.

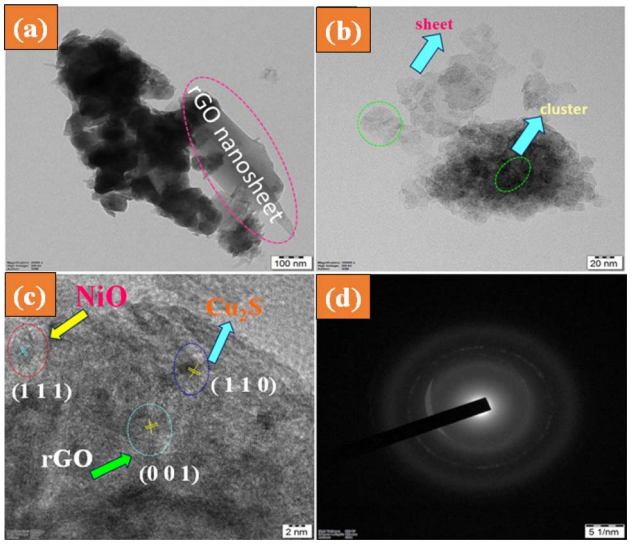


Fig. 4 (a)–(c) HR-TEM images of the ternary nanocomposite NiO/$Cu_2S$/rGO processed at different magnifications; (d) SAED pattern.

nanosheets is expected to enhance the charge carrier recombination rates. This result indicates that the NiO/$Cu_2S$/rGO ternary nanocomposites affirm the heterojunction formation.

### 3.5 Electrocatalytic activity

**3.5.1 Cyclic voltammetry.** Cyclic voltammetry experiments were carried out to gain deeper insights into the interactions taking place between the modified electrodes and the electrolyte. The CV characteristics of the bare GCE, NiO/GCE, rGO/GCE, $Cu_2S$/GCE, NiO/$Cu_2S$/GCE and NiO/$Cu_2S$/rGO/GCE nanocomposite were explored in a 5 mM of $[Fe(CN)_6^{3-}]$ electrolyte solution. Fig. 5(a) shows the well-defined CV curves revealed to the reversible redox peak reaction of $[Fe(CN)_6^{3-}]$ on the surface of the GCE working electrode. The anodic peak current of NiO/$Cu_2S$/rGO/GCE nanocomposite significantly increased compared to those of bare GCE, GCE/NiO, GCE/rGO, GCE/$Cu_2S$ and NiO/$Cu_2S$/GCE, which clearly confirmed that NiO/$Cu_2S$/rGO/GCE nanocomposites have good electrocatalytic activity and enhanced the electron transfer ratio of potassium ferricyanide on the working electrode surface. Fig. 5(b) shows the

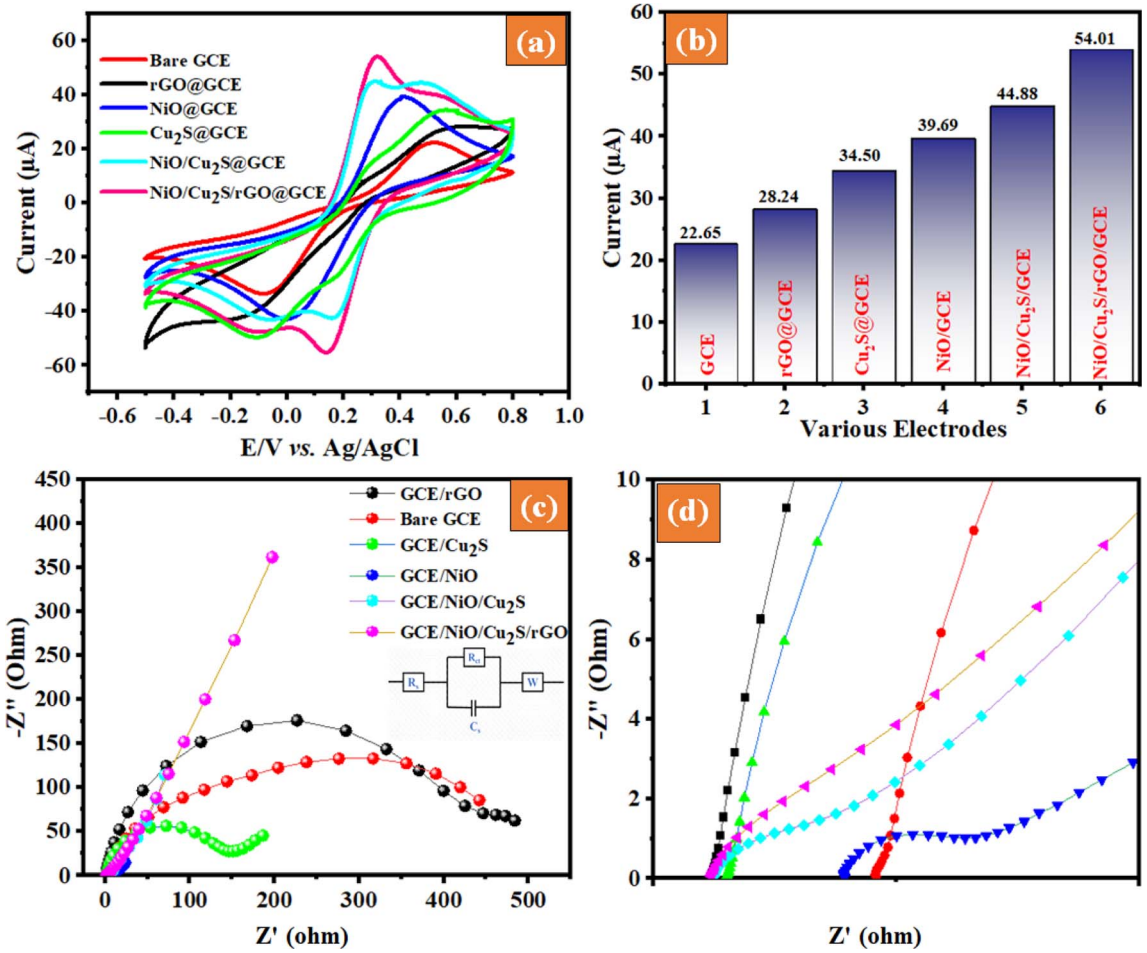


Fig. 5 (a) Cyclic voltammetry (CV) spectra and scan rate of the 50 mV $s^{-1}$, (b) corresponding bar diagram, (c) EIS – Nyquist plot, and (d) inset full view of the respective electrodes.

equivalent histogram of the current response of the as-prepared sample pure GCE, GCE/NiO, GCE/rGO, GCE/$Cu_2S$, NiO/$Cu_2S$/GCE and NiO/$Cu_2S$/rGO/GCE were measured to be 22.65, 28.24, 34.50, 39.69, 44.88 and 54.01 μA, respectively.

**3.5.2 Electrochemical impedance spectroscopy.** The kinetics of interfacial reactions in the electrochemical system were studied using electrochemical impedance spectroscopy (EIS). EIS is a very reliable and simple technique for investigating electrode response, charge transfer resistance, and interfacial interaction in as-prepared modified electrodes. As illustrated in Fig. 5(c), EIS analysis of the as-prepared bare GCE, NiO/GCE, rGO/GCE, $Cu_2S$/GCE, NiO/$Cu_2S$/GCE and NiO/$Cu_2S$/rGO/GCE modified electrodes were studied in 5 mM of $[Fe(CN)_6^{3-}]$. The signal amplitude is 5 mV, and its frequency ranges from 0.1 to 100 kHz. In Fig. 5(d), which consists of two portions, a destroyed linear and semicircle portion, the diameter of the semicircle region is deemed to be equal to the electron transfer resistance ($R_{ct}$) at the modified electrode surface, and the linear part shows the diffusion-controlled process that supports the capacitive behaviour of the electrode. Fig. 5(d) shows that the vertical portion is virtually 45°, suggesting ion transport to the interior electrolyte of the electrode layer. However, with the production of a ternary nanocomposite, the semicircle is reduced by bending the linear component to a more vertical position, suggesting improved conducting behaviour and lower resistive nature. The smaller semicircle observed in NiO/$Cu_2S$/rGO/GCE nanocomposite compared to bare and composite-modified electrodes indicates that the ternary composite has a lower charge transfer resistance. According to the above results, the lowest $R_{ct}$ value obtained for NiO/$Cu_2S$/rGO/GCE electrodes indicates improved electrocatalytic activity and high interfacial electron transfer ability.

## 3.6 Photocatalytic application

**3.6.1 RhB and MB dye degradation.** The photocatalytic degradation activity of the as-prepared photocatalysts was investigated by determining the degradation rates of various dyes, such as RhB, MB, and mixed dyes, under UV-visible light irradiation. To conduct the experiments, we choose the following reaction parameters: 100 mg of catalyst, 27 °C temperature, pH 7.0, and dye concentration 10 ppm. When tested under visible light in the absence of a photocatalyst, we found that MB, RhB, and mixed dye solutions (RhB and MB) remained quite stable. We did not observe a decrease in dye concentration after 30 min of the photolysis process. The UV-visible absorption spectra of the undecomposed RhB and MB dye solutions during the photocatalytic reaction under UV-light irradiation with different catalysts were used. Fig. 6(a) and 7(a) indicate that the removal efficiency of the NiO/$Cu_2S$/rGO ternary nanocomposites for RhB dye and MB dye gradually decreased over time. In Fig. 6(b) and 7(b), the changes in RhB and MB dye concentration ($C/C_0$) with reaction time are illustrated. The RhB and MB dyes exhibited degradation efficiencies of only 3% and 4.2%, respectively. This denotes that the self-degradation effect of RhB and MB dye was almost negligible under UV-light irradiation. To elaborate, the adsorption of RhB and MB dye on the different photocatalysts reached an equilibrium condition within 30 min under dark conditions. Consequently, when NiO

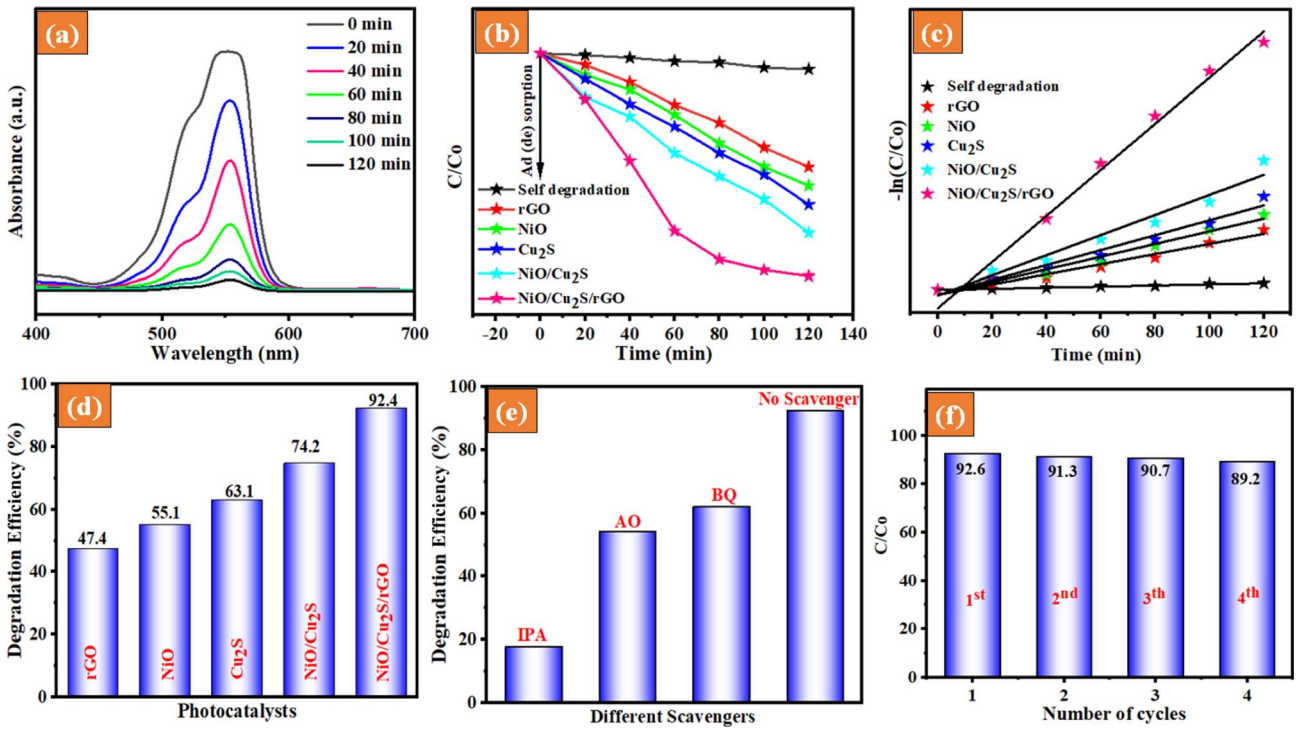


Fig. 6 UV-visible absorption spectra of (a) RhB dye solution containing ternary NiO/$Cu_2S$/rGO nanocomposites, (b) relative concentration ($C/C_0$) *versus* time (min), (c) pseudo-first-order kinetic plot, (d) degradation efficacy, (e) scavenger experiment and (f) recyclability of the as-prepared NiO/$Cu_2S$/rGO ternary nanocomposites.

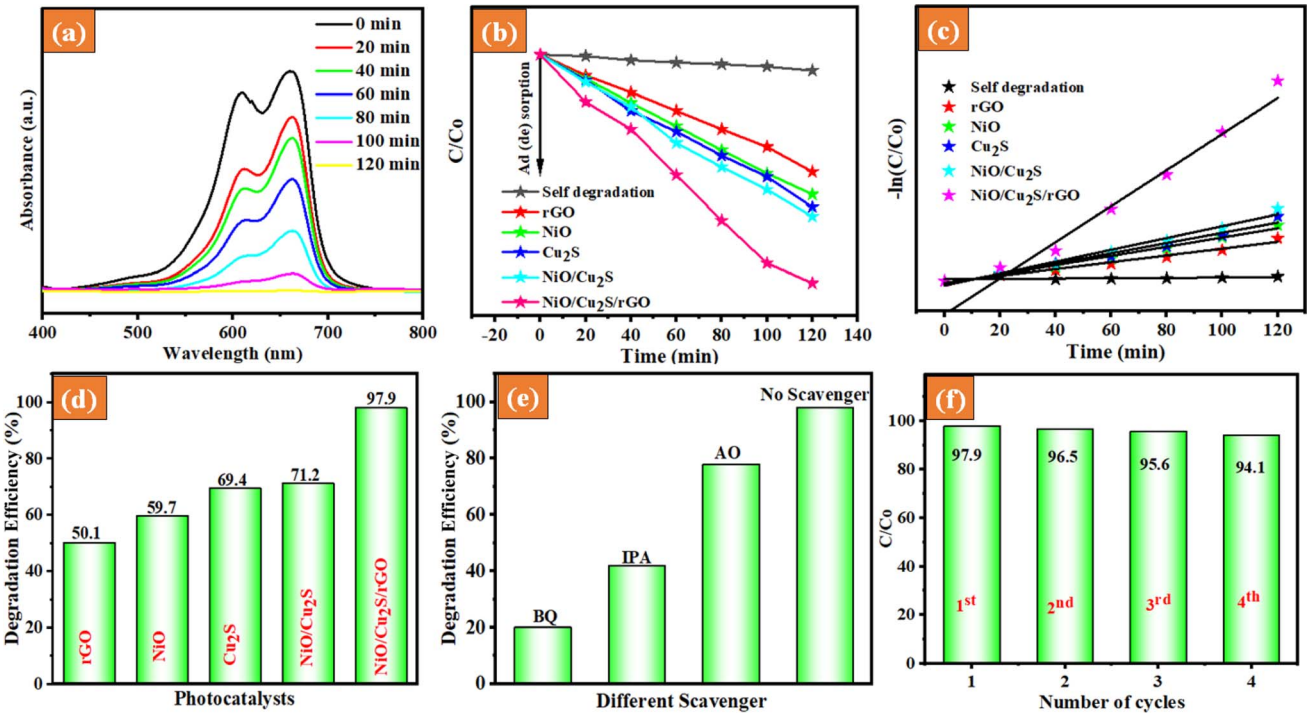


Fig. 7 UV-visible absorption spectra of (a) MB dye solution contain $NiO/Cu_2S/rGO$ ternary nanocomposites, (b) relative concentration ($C/C_0$) *versus* time (min), (c) pseudo-first-order kinetic plot, (d) degradation efficacy, (e) scavenger and (f) recyclability of the as-prepared ternary $NiO/Cu_2S/rGO$ nanocomposites.

nanoparticles were introduced into the RhB and MB dye solutions, the degradation of RhB and MB dye increased to 55.1 and 59.7% efficiency, respectively. When $Cu_2S$ nanoparticles were present in the same solution, the degradation efficiency reached 63.1% for RhB and 69.4% for MB under the same UV-light irradiation. However, these results were not satisfactory. Moreover, it is discovered that the addition of rGO nanosheets leads to an increase in degradation efficiency. The RhB dye and MB dye degradation for the $NiO/Cu_2S/rGO$ ternary nanocomposites reached 92.4% and 97.9% efficiency after 120 min under UV-visible light irradiation, respectively. For further investigation, the Langmuir–Hinshelwood formula was employed to analyze the reaction kinetics:

$$\ln(C/C_0) = k_{app}t,$$

where $C_0$ = initial concertation of RhB and MB dyes, $C$ = final concertation of RhB and MB dyes, and $t$ = time.

The first-order linear fit curves provide the value of $k_{app}$, as illustrated in Fig. 6(c) and 7(c). These results indicate that the $NiO/Cu_2S/rGO$ ternary nanocomposites have increased photocatalytic degradation activity, accomplished by significant light absorption and effective charge separation. Fig. 6(d) and 7(d) show the photodegradation efficiency of different as-prepared photocatalysts. The $NiO/Cu_2S/rGO$ ternary nanocomposites performed better in terms of degradation efficiency than the other bare and composites. To analyze the surface reaction mechanism pathway of $NiO/Cu_2S/rGO$ ternary nanocomposites, scavenger experiments were conducted in the RhB dye degradation process system. Three radical scavengers, namely isopropanol (IPA), benzoquinone (BQ) and ammonium oxalate (AO) as scavengers of ($^{\bullet}OH$), ($O_2^{\bullet-}$) radicals and $h^+$ were added to the degradation process, respectively. The results are displayed in Fig. 6(e) and 7(e). However, the $NiO/Cu_2S/rGO$ ternary nanocomposites were subjected to the same scavenger experiment under MB dye degradation. Based on the above results, the RhB and MB dyes were found to be involved in the hydroxyl ($^{\bullet}OH$) and superoxide radical ($O_2^{\bullet-}$), highly contributing to the photocatalytic reactions.

**3.6.2 Mixed dye degradation.** The mixed dye degradation behaviour of the as-prepared photocatalysts was evaluated using mixed organic pollutant dyes (MB and RhB). The photodegradation ability of the as-prepared nanocomposites was observed at maximum absorption peaks around 565 and 664 nm for the RhB and MB dyes, respectively. Notably, the UV absorption spectra of the MB and RhB dye molecules decreased simultaneously, as shown in Fig. 8(a). As depicted in Fig. 8(b), the $NiO/Cu_2S/rGO$ ternary nanocomposites exhibited the highest removal efficiency of 91.6%, surpassing other bare and other composites, including NiO, $Cu_2S$, rGO, and $NiO/Cu_2S$, which had dye removal efficiencies of 49.5, 52, 45 and 61%, respectively. This enhanced performance can be attributed to the improved visible light harvesting efficiency and dense active sites, which are crucial for the segregation and transfer of photoexcitons at the interface between NiO, $Cu_2S$, and rGO nanosheets.

**3.6.3 Kinetic study.** The kinetic activity of the as-prepared samples for the photocatalytic degradation of RhB and MB

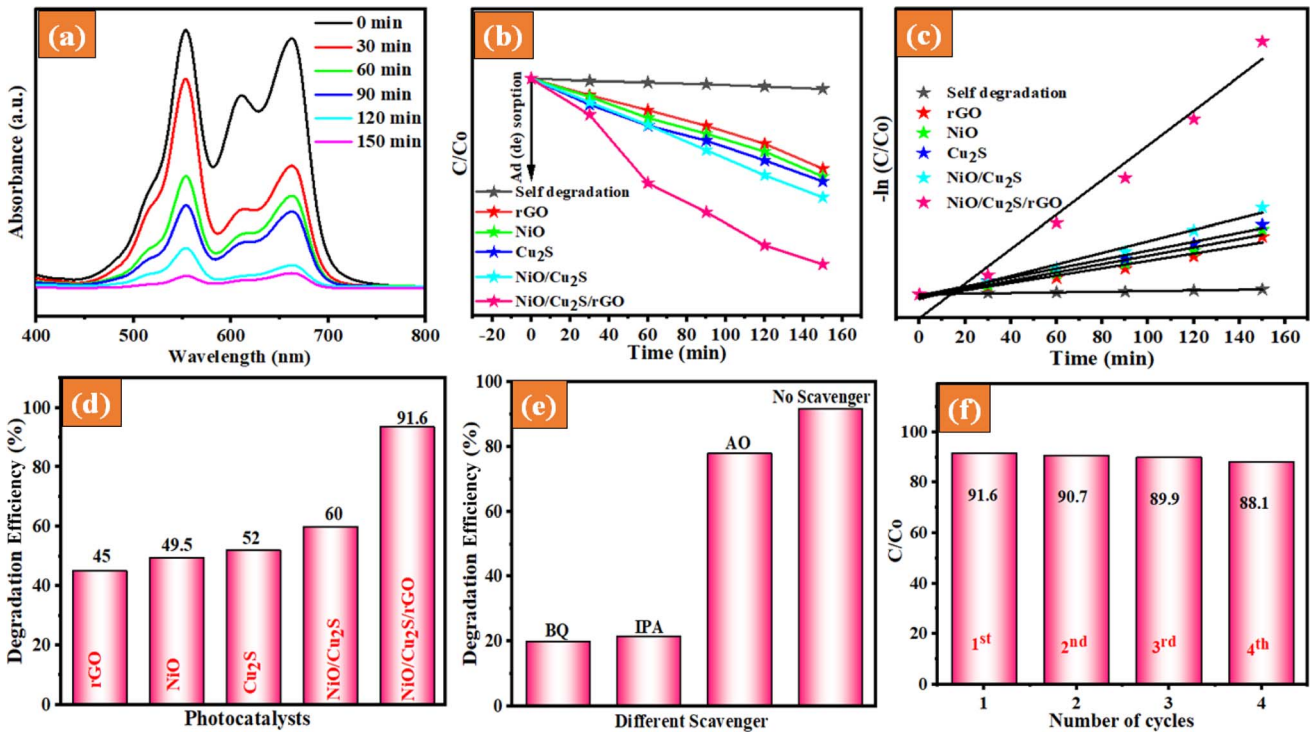


Fig. 8 UV-visible absorption spectra of (a) RhB and MB dye solution containing NiO/$Cu_2S$/rGO ternary nanocomposites, (b) relative concentration ($C/C_0$) *vs.* time (min), (c) pseudo-first-order kinetic plot, (d) degradation efficacy, (e) scavenger and (f) recyclability of the as-prepared NiO/$Cu_2S$/rGO ternary nanocomposites.

dyes was investigated using the Langmuir–Hinshelwood model. It was found that the photocatalytic degradation process followed pseudo-first-order kinetics, as depicted in Fig. 8(c). Based on the above results, the rate constants ($k_{app}$) were calculated, and the obtained rate constant values are 0.00941, 0.00743, 0.0143, 0.0143, 0.0181, and 0.0230, corresponding to rGO, NiO, $Cu_2S$, NiO/$Cu_2S$ and NiO/$Cu_2S$/rGO ternary nanocomposites, respectively. The rate constant of NiO/$Cu_2S$/rGO ternary nanocomposites is up to 2.15-fold faster than that of the bare NiO. In Table 1, provides a detailed elaboration of several validation parameters and various synthetic methods as documented in the previous report.

**3.6.4 Scavenger study.** To understand the main active species responsible for RhB and MB dye degradation, free radical trapping experiments were conducted by adding various scavengers to the ternary NiO/$Cu_2S$/rGO nanocomposite. The results are displayed in Fig. 8(e). In this experiment, 1 mM of BQ, 1 mM of IPA and 1 mM of AO were utilized for quenching ($O_2^{\bullet-}$), ($^{\bullet}OH$) and electron holes, respectively. Based on these findings, ($O_2^{\bullet-}$) and ($^{\bullet}OH$) radicals play a significant role during the photocatalytic process under UV-visible light irradiation.

**3.6.5 Photocatalytic degradation mechanism.** Fig. 9 shows the proposed tentative mechanism of MB, RhB, and mixed dye (RhB and MB) degradation by NiO/$Cu_2S$/rGO ternary nanocomposites. According to the energy band gap, it is clearly denoted that all pure photocatalyst materials can absorb visible light. The valence band and conduction band edge potential of the as-prepared sample are calculated using the following eqn (1) & (2):

$$E_{CB} = \chi - E_0 - 0.5E_{gap}, \quad (1)$$

$$E_{VB} = E_{CB} + E_{gap}, \quad (2)$$

Table 1 Comparison of the photodegradation activity of NiO/$Cu_2S$/rGO ternary nanocomposites with other related materials

| S. no. | Photocatalysts | Synthetic method | Model pollutant | Time (min) | Light source | Degradation efficiency (%) | Ref. |
|---|---|---|---|---|---|---|---|
| 1 | Fe doped NiO | Co-precipitation | MB | 60 | Sun light | 86 | 41 |
| 2 | $MnO_2$/NiO–Ag | Combustion method | MB | 120 | 500 W Xe lamp | 91.25 | 42 |
| 3 | $Fe_2O_3$–NiO | Hydrothermal method | RhB | 100 | Visible light | 96 | 43 |
| 4 | rGO/NiO/$TiO_2$ | Sol–gel method | MB | 180 | 500 W Xe lamp | 88 | 44 |
| 5 | NiO/$Cu_2S$/rGO | Hydrothermal method | RhB and MB | 150 | 500 W Xe lamp | 91.1 | Our work |

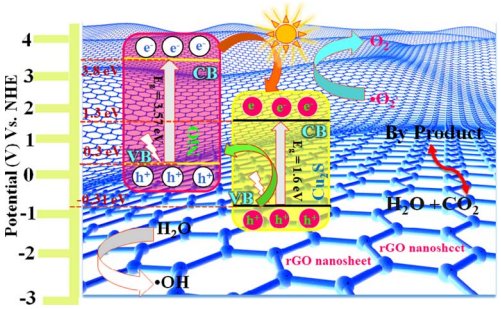


Fig. 9 Schematic illustration of the proposed photocatalytic degradation mechanism pathway of the NiO/$Cu_2S$/rGO ternary nanocomposites.

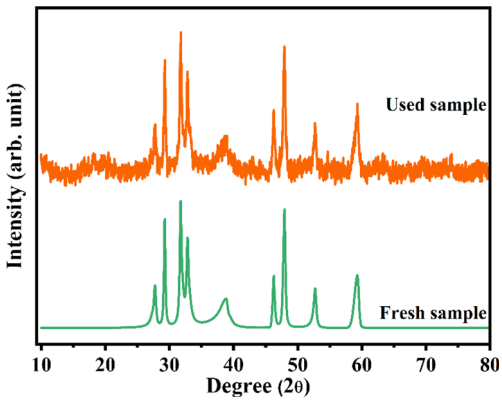


Fig. 10 Reusability of the as-prepared NiO/$Cu_2S$/rGO ternary nanocomposites.

where $\chi$ is the electronegativity values of the corresponding photocatalysts, $E_{gap}$ is the energy band gap of the as-prepared material, and $E_{CB}$ and $E_{VB}$ are the conduction band and valence band edge positions of the semiconductor, respectively.[45] The absolute electronegativity values of the NiO and $Cu_2S$ nanoparticles are 6.585 and 5.00 eV, respectively. Substituting these parameters into the above equation, the CB positions of NiO and $Cu_2S$ are 3.8 and 1.3 eV and the VB positions are 0.3 and −0.31 eV, respectively. The CB position of NiO was more positive than that of the CB position of $Cu_2S$, so the photogenerated electrons easily migrated from the CB of the NiO nanoparticles to the CB band of $Cu_2S$. Furthermore, the above scavenger's result demonstrates that during the photocatalytic reaction, electrons can be captured by ($O_2$) to create a superoxide radical ($O_2^{\bullet -}$) anion. However, holes can be captured by OH to create hydroxyl radicals (•OH), leading to the degradation of mixed and individual dyes. The diagram indicates that superoxide and hydroxide radicals are effectively separated from each other on the surface of the NiO/$Cu_2S$/rGO ternary nanocomposites. The following equations describe the photocatalytic reactions of NiO/$Cu_2S$/rGO ternary nanocomposites:

$$\text{NiO/Cu}_2\text{S/rGO} + h\nu \rightarrow \text{NiO/Cu}_2\text{S/rGO}\ (e^- + h^+) \quad (3)$$

$$\text{NiO/Cu}_2\text{S/rGO}\ (e^- + h^+) \rightarrow \text{rGO}\ (e^- + h^+) + \text{NiO}\ (e^- + h^+) + \text{Cu}_2\text{S}\ (e^- + h^+) \quad (4)$$

$$\text{NiO}\ (e^-) + \text{Cu}_2\text{S}\ (e^-) + O_2 \rightarrow (O_2^{\bullet -}) \quad (5)$$

$$\text{rGO}\ (h^+) + H_2O \rightarrow (^{\bullet}OH) + H \quad (6)$$

$$O_2^{\bullet -} + (\text{MB}) \rightarrow \text{intermediate } CO_2 + H_2O + (\text{decomposed products}) \quad (7)$$

$$(^{\bullet}OH) + (\text{RhB}) \rightarrow \text{intermediate } CO_2 + H_2O + (\text{decomposed products}) \quad (8)$$

$$OH^{\bullet} + \text{mixed (RhB and MB)} \rightarrow \text{intermediate } CO_2 + H_2O + (\text{decomposed products}) \quad (9)$$

**3.6.6 Recyclability and stability of the NiO/$Cu_2S$/rGO ternary nanocomposites.** Reusability is an essential parameter for environmental applications. Based on the above description, NiO/$Cu_2S$/rGO ternary nanocomposites demonstrate potential as efficient and promising photocatalysts. Stability and recyclability play crucial roles in the photocatalytic performance of the as-prepared materials. After the photodegradation process, NiO/$Cu_2S$/rGO ternary nanocomposites were collected from the RhB and MB dye solutions and purified using a previous procedure. As shown in Fig. 6(f), 7(f) and 8(f) over four consecutive runs, there were only minor differences in photocatalytic ability after four consecutive cycles compared to the first cycle. However, during the repeated purification procedure to separate the materials from the RhB, MB, and mixed (RhB and MB) dye solutions, a decrease in photocatalytic efficiency was observed. The small variation in photocatalytic activity during each cycle is likely due to the aggregation of the as-prepared samples during the photocatalytic degradation process. Fig. 10 depicts NiO/$Cu_2S$/rGO ternary nanocomposites before and after the photocatalytic experiments, indicating that there was no notable change in peak shape, and no additional peak emerged. These results reveal that the NiO/$Cu_2S$/rGO ternary nanocomposites exhibit good stability.

## 4. Conclusion

In summary, a simple one-pot hydrothermal approach is initially developed for the preparation of the NiO/$Cu_2S$/rGO ternary nanocomposites utilized to degrade individual RhB, MB dye and mixed (RhB and MB) dyes. The as-prepared samples underwent analysis of various physical, chemical and optical properties. Particularly, HRTEM analysis was employed to determine the strong interaction between the nanoparticles, denoted by the heterojunction formation of the as-prepared NiO/$Cu_2S$/rGO ternary nanocomposites. More importantly, the electrocatalytic properties of the prepared samples were elucidated through EIS and CV measurements. EIS provided insights into the interfacial charge transfer resistance and electron transfer kinetics, while CV analysis offered valuable information regarding the redox behaviour and overall electrochemical

characteristics of the photocatalyst. Consequently, the NiO/$Cu_2S$/rGO ternary nanocomposites exhibit superior photocatalytic properties, high stability, and good reproducibility in catalyzing the decomposition of individual and mixed dyes under visible light irradiation. Consequently, the prepared NiO/$Cu_2S$/rGO ternary nanocomposites are well attuned to ($^{\bullet}OH$) and ($O_2^{\bullet-}$) radicals during the experiments. Moreover, the recycling and stability test confirms the robust stability of the as-prepared NiO/$Cu_2S$/rGO ternary nanocomposites. Hence, the NiO/$Cu_2S$/rGO ternary nanocomposites demonstrate promising potential as photocatalyst materials for wastewater treatment and environmental applications.

## Author contributions

Balaji Parasuraman: conceptualization, investigation, writing – original draft; Paramasivam Shanmugam: data curation, formal analysis; Sangaraju Sambasivam: methodology, data curation, visualization; Hariprasath Rangaraju: visualization, investigation formal analysis; Dhayalss Raj Alphonse: data curation, conceptualization; Mohammad Nawaz Husain: validation, investigation, formal analysis; Pazhanivel Thangavelu: supervision, visualization, project administration, formal analysis.

## Conflicts of interest

The authors declare that there is no conflict of interest regarding the publication of this manuscript.

## References

1 H. Dihingia, S. Pathak, Lalmalsawmdawngliani, Lalhmunsiama, D. Tiwari and D.-J. Kim, *J. Taiwan Inst. Chem. Eng.*, 2023, 105096.
2 C. H. Nguyen, T. T. Van Tran, M. L. Tran and R.-S. Juang, *J. Taiwan Inst. Chem. Eng.*, 2023, **145**, 104825.
3 P. Shanmugam, R. C. Ngullie, S. Meejoo Smith, S. Boonyuen, R. Boddula and R. Pothu, *Mater. Sci. Energy Technol.*, 2023, **6**, 359–367.
4 M. Jaishankar, T. Tseten, N. Anbalagan, B. B. Mathew and K. N. Beeregowda, *Interdiscip. Toxicol.*, 2014, **7**, 60–72.
5 M. Bilal, I. Ihsanullah, M. U. Hassan Shah, A. V. Bhaskar Reddy and T. M. Aminabhavi, *J. Environ. Manage.*, 2022, **321**, 115981.
6 Z. Mulushewa, W. T. Dinbore and Y. Ayele, *Environmental Analysis Health and Toxicology*, 2021, **36**, e2021007.
7 S. Venkatesh, K. Venkatesh and A. R. Quaff, *J. Appl. Res. Technol.*, 2017, **15**, 340–345.
8 N. Tanwar, V. Dhiman, S. Kumar and N. Kondal, *Mater. Today: Proc.*, 2022, **48**, 1401–1406.
9 S. C. M. Signorelli, J. M. Costa and A. F. de Almeida Neto, *J. Environ. Chem. Eng.*, 2021, **9**, 106157.
10 S. F. Anis, B. S. Lalia, A. Lesimple, R. Hashaikeh and N. Hilal, *Chem. Eng. J.*, 2022, **428**, 131184.
11 M. H. Pinoargote-Chang, A. Fernández-Andrade, L. A. Zambrano-Intriago, L. S. Quiroz-Fernández, G. Villanueva-Ramos, M. C. B. S. M. Montenegro and J. M. Rodríguez-Díaz, *Case Stud. Chem. Environ. Eng.*, 2022, **6**, 100226.
12 K. Okitsu, K. Iwasaki, Y. Yobiko, H. Bandow, R. Nishimura and Y. Maeda, *Ultrason. Sonochem.*, 2005, **12**, 255–262.
13 F. Mcyotto, Q. Wei, D. K. Macharia, M. Huang, C. Shen and C. W. K. Chow, *Chem. Eng. J.*, 2021, **405**, 126674.
14 G. Chandrabose, A. Dey, S. S. Gaur, S. Pitchaimuthu, H. Jagadeesan, N. S. J. Braithwaite, V. Selvaraj, V. Kumar and S. Krishnamurthy, *Chemosphere*, 2021, **279**, 130467.
15 V. Golob, A. Vinder and M. Simonic, *Dyes Pigm.*, 2005, **67**, 93–97.
16 A. V. Mohod, M. Momotko, N. S. Shah, M. Marchel, M. Imran, L. Kong and G. Boczkaj, *Water Resour. Ind.*, 2023, **30**, 100220.
17 R. C. Ngullie, K. Bhuvaneswari, P. Shanmugam, S. Boonyuen, S. M. Smith and M. Sathishkumar, *Catalysts*, 2022, **12**, 1073.
18 B. Parasuraman, B. Kandasamy, I. Murugan, M. S. Alsalhi, N. Asemi, P. Thangavelu and S. Perumal, *Chemosphere*, 2023, **334**, 138979.
19 P. Shanmugam, B. Parasuraman, S. Boonyuen, T. Pazhanivel, S. A. Mohamad, L. T. Z. Alvin and A. Viji, *Environ. Geochem. Health*, 2024, **46**, 92.
20 E. Amdeha, 2023, 112–154.
21 R. Pelalak, A. Hassani, Z. Heidari and M. Zhou, *Chem. Eng. J.*, 2023, **474**, 145511.
22 E. Amdeha and M. Salem, *Egypt. J. Chem.*, 2022, **65**(132), 557–569.
23 Z. Mirzaeifard, Z. Shariatinia, M. Jourshabani and S. M. Rezaei Darvishi, *Ind. Eng. Chem. Res.*, 2020, **59**, 15894–15911.
24 F. Motahari, M. R. Mozdianfard, F. Soofivand and M. Salavati-Niasari, *RSC Adv.*, 2014, **4**, 27654.
25 C. N. C. Hitam and A. A. Jalil, *J. Environ. Manage.*, 2020, **258**, 110050.
26 P. Raizada, A. Sudhaik, S. Patial, V. Hasija, A. A. Parwaz Khan, P. Singh, S. Gautam, M. Kaur and V.-H. Nguyen, *Arabian J. Chem.*, 2020, **13**, 8424–8457.
27 V. Mahdikhah, S. Saadatkia, S. Sheibani and A. Ataie, *Opt. Mater.*, 2020, **108**, 110193.
28 A. Shokri, *Environ. Challenges*, 2021, **5**, 100332.
29 R. A. El-Salamony, E. Amdeha, A. M. El Shafey and A. M. Al Sabagh, *Int. J. Environ. Anal. Chem.*, 2023, **103**, 868–883.
30 B. Parasuraman, V. Vasudevan, B. Kandasamy, H. Rangaraju and P. Thangavelu, *Environ. Sci. Pollut. Res.*, 2023, DOI: 10.1007/s11356-023-26627-9.
31 S. Vignesh, G. Palanisamy, M. Srinivasan, N. Elavarasan, K. Bhuvaneswari, G. Venkatesh, T. Pazhanivel, P. Ramasamy, M. A. Manthrammel and M. Shkir, *Diamond Relat. Mater.*, 2021, **120**, 108606.
32 J. Jia, Q. Zhang, K. Li, Y. Zhang, E. Liu and X. Li, *Int. J. Hydrogen Energy*, 2023, **48**, 196–231.
33 M. Shkir, T. H. AlAbdulaal, M. Ubaidullah and V. Reddy Minnam Reddy, *Chemosphere*, 2023, **338**, 139432.
34 X. Wang, G. Yang, G. Chai, M. S. Nasir, S. Wang, X. Zheng, C. Wang and W. Yan, *Int. J. Hydrogen Energy*, 2020, **45**, 30634–30646.

35 S. Li, X. Hao, X. Dai and T. Tao, *J. Nanomater.*, 2018, **2018**, 1–12.
36 J. K. Kim, *Polymers*, 2019, **11**, 120.
37 B. Parasuraman, V. Vasudevan, B. Kandasamy, H. Rangaraju and P. Thangavelu, *Environ. Sci. Pollut. Res.*, 2023, DOI: 10.1007/s11356-023-26627-9.
38 P. S. Kumar and S. Goel, *Diamond Relat. Mater.*, 2021, **120**, 108680.
39 F. Dai, Q. Zhuang, G. Huang, H. Deng and X. Zhang, *ACS Omega*, 2023, **8**, 17064–17076.
40 B. Kandasamy, P. Govindasamy, P. Thangavelu, J. Theerthagiri, A. Min and M. Y. Choi, *Chemosphere*, 2022, **290**, 133299.
41 A. Khatri and P. S. Rana, *Phys. B*, 2020, **579**, 411905.
42 S. Parameswaran, R. Bakkiyaraj, P. Shanmugam and T. Venugopal, *Chem. Phys.*, 2023, **575**, 112077.
43 S. Khan, Z. Ajmal, S. Mahmood and M. ul Haq, *New J. Chem.*, 2023, **47**, 10333–10346.
44 K. Santhosh, S. SK, S. Chouti, S. Gonuguntla, S. P. Ega, A. Tiwari and U. Pal, *J. Mol. Struct.*, 2021, **1235**, 130222.
45 G. Palanisamy, K. Bhuvaneswari, J. Lee, A. Viji and M. Shkir, *Spectrochim. Acta, Part A*, 2024, **304**, 123400.